

## Analysing effective thermal conductivity of 2D closed-cell foam based on shrunk Voronoi tessellations

H. WANG<sup>1,2)</sup>, B. LIU<sup>1)</sup>, Y.-X. KANG<sup>1)</sup>, Q.-H. QIN<sup>2)</sup>

<sup>1)</sup>*College of Civil Engineering & Architecture  
Henan University of Technology  
Zhengzhou, 450001, China  
e-mail: huiwang@haut.edu.cn*

<sup>2)</sup>*Research School of Engineering  
Australian National University  
Canberra, 2016, Australia  
e-mail: qinghua.qin@anu.edu.au*

TWO-DIMENSIONAL FOAM IS A TYPE of cellular solid materials containing a high volume fraction of pores. The thermal behavior of foam depends strongly on its microscopic structure. In this study, a two-dimensional closed-cell foam model containing randomly distributed air voids and solid walls is designed via a Voronoi diagram enhanced by the shrinking technique to approximately represent the real foam structure. The porosity, pore size and solid wall thickness of the established random foam structure is examined by introducing the so-called shrinking ratio. Subsequently, the effective thermal conductivity of the rebuilt foam model is numerically presented through the finite element analysis. The numerical results obtained are verified by comparison with the available theoretical and experimental results. In the analysis, the effects of porosity, number of pores and thermal conductivity of solid phase in foam structures are investigated respectively to reveal the relationship of geometric parameters and thermal properties of solid phase with effective thermal conductivity of the foam.

**Key words:** closed-cell foam, microstructure, Voronoi tessellation, shrinking ratio, effective thermal conductivity.

Copyright © 2017 by IPPT PAN

### 1. Introduction

THE VORONOI TESSELLATION OR VORONOI DIAGRAM is generated by constructing the perpendicular bisectors of pairs of adjacent points and thus each cell possesses several connected neighbors. Because of this distinctive feature, the Voronoi tessellation with random polygonal cells has been directly applied to mesh complex geometries with various convex polygons [1–4]. As a type of cellular solid materials, a real foam structure including closed-cell or open-cell foam usually possesses random and complex geometric morphology such as nu-

merous and disordered pores or cells, irregular cell shape, and nonuniform cell walls [5]. Originally the random Voronoi tessellation is suitable for geometrically reproducing foam structures at microstructure level. The Voronoi tessellation and more particularly the Laguerre–Voronoi tessellation have recently been proposed to reconstruct two-dimensional (2D) and three-dimensional (3D) foam microstructures [6–12].

When the irregularity of pore shapes, the randomness of pore locations and the interaction of pores are incorporated in foam structures, analytical analysis becomes impractical and the use of numerical methods, mainly the finite element method, is appropriate. The combination of the Voronoi tessellation and the finite element technique has been widely used to study the mechanical and thermal properties of the 2D foam materials. For example, SILVA *et al.* [13] numerically studied the elastic properties of non-periodic microstructure of 2D cellular solids with the help of the Voronoi diagram and the finite element technique, and subsequently they examined the effects of non-periodic microstructure and defects on the compressive strength of 2D cellular solids [14]. CHEN *et al.* [15] investigated the influence of six different imperfections on the yielding of 2D foams using the finite element method. ZHU *et al.* [16] constructed periodical 2D Voronoi foam structures with different degrees of irregularity and determined their effective elastic properties by applying the finite element analysis. LI *et al.* [12] established the 2D Voronoi cellular solid models based on a modified Voronoi tessellation technique and studied their negative Poisson's ratio by using the finite element method. TANG *et al.* [7] investigated the effects of cell size and shape irregularity on mechanical properties of 2D and 3D Voronoi foams using the finite element analysis. In addition to the mechanical properties, the thermal-physical properties of metallic foams also play a significant role in modeling the heat transfer phenomena in foam materials for designing new porous media. In this field, LU and CHEN [17] calculated the apparent thermal conductivity of 2D closed-cell aluminum alloy foam with various microstructures including regular honeycomb, Voronoi structures and the Johnson–Mehl model by means of finite element technique. LU *et al.* [18] developed a finite element model of 2D closed-cell aluminum foam with circular pores and numerically investigated the effect of the distribution of circular pores on the effective thermal property of the foam. LI *et al.* [9] established 2D and 3D Voronoi finite element models for simulating thermal properties of closed-cell metal foams with different cell shape irregularity. However, little study on thermal properties of metallic foam was conducted by using both the Voronoi tessellation and the finite element method, and local morphological parameters of both pore and solid phases in real foam structures were not fully discussed. Thus, it is necessary to conduct further investigation in this area.

In this work, in order to quantitatively investigate thermal property of real closed-cell foam, a simple and efficient shrinking algorithm of Voronoi tessellation

is developed for producing 2D virtual microstructure of its statistically equivalent counterpart with randomly distributed polygonal pores that are closed-packed and non-overlapping. Practically, the statistically equivalent counterpart of a real foam can be understood as an approximate replacement of the actual scanned image of a real foam sample in which the size, shape and quantity of pores and the wall thickness between neighboring pores can be experimentally measured and then counted and averaged for data statistics, as illustrated for the geometrical rebuilt of two-phase ceramic composite [19] and closed-cell aluminum foams [20]. The shrinking technique allows us to produce controllable local-geometrical-morphology of any particular polygonal pore through a specific shrinking ratio and thus provides an opportunity to create various virtual foams with precisely controllable parameters including porosities, number of pores and thickness of solid walls. In order to evaluate thermal conductivities of the foams that have different porosities (i.e. 55%–95%), the finite element technique is employed to solve the energy balance equations of heat transfer in the foams for both solid and air phases. The results are validated against available theoretical predictions and experimental results.

## **2. Generation of closed-cell foam structure with shrunk Voronoi tessellations**

Since it is difficult to study numerically the complicated real foam structure directly, building an acceptable geometric model to serve as an idealized representative volume element (RVE), to represent the microstructural features of a non-periodic real foam material is a key issue for microstructure analysis of such a material. Currently, the methods of reconstructing a foam structure include mainly the computed tomography (CT) scanning technology [21–23] and the Voronoi tessellation (VT) technology [9, 10, 12]. The CT scanning technology can reproduce a geometric representation mostly close to the actual foam structure by using numerous scanning images of the sample with specified porosity, but it usually requires strong capability of image post-processing. Further, the efficiency and accuracy of reconstruction model strongly depends on the CT scanning resolution. Different from the CT scanning technology, the Voronoi tessellation technology is a virtual approximate reconstruction of a real foam structure over Voronoi tessellations to provide a full control of microstructure. One can flexibly adjust microstructure and porosity of virtual foam manually using numerous geometrical tessellations to represent morphological imperfections in real foam materials [6, 13, 24, 25].

In this section, the Voronoi tessellation method is employed to generate the approximate Voronoi diagram of actual foam with the same number of pores and domain dimensions, and then the 2D virtual closed-cell foam structure with

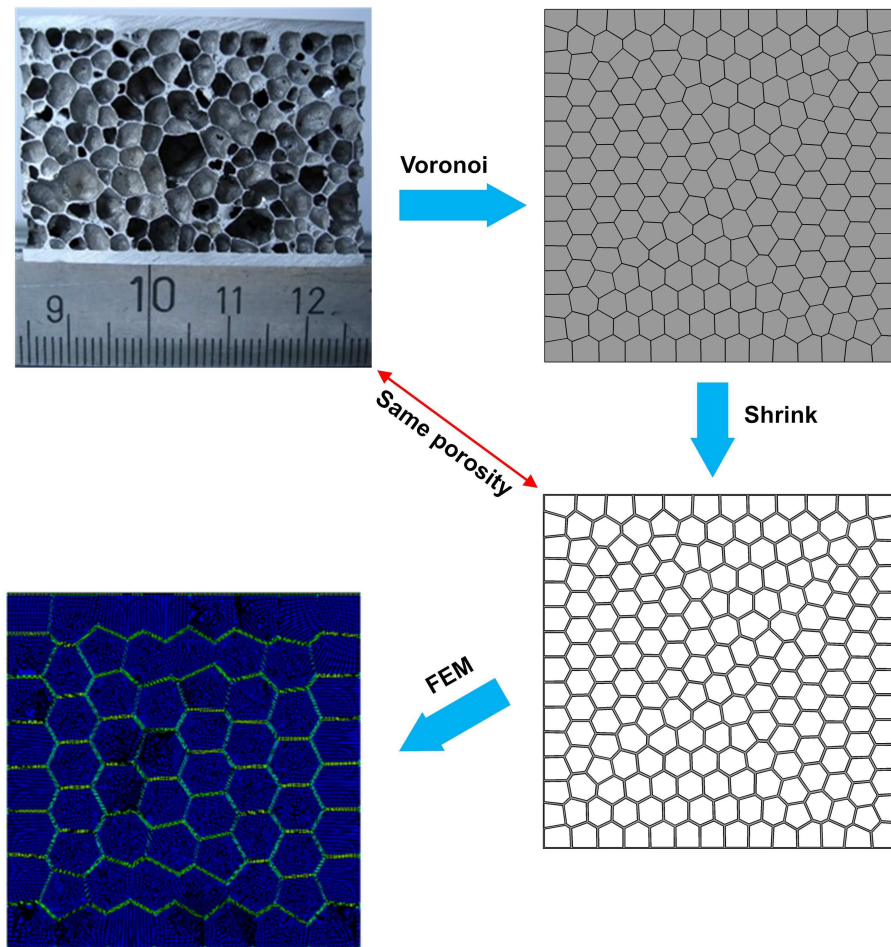


FIG. 1. The basic reconstruction process with shrunk Voronoi tessellations.

controllable morphological parameters is constructed through the shrinking of the Voronoi diagram for the follow-up finite element thermal analysis. The basic reconstruction process is shown in Fig. 1. It is worth noting that only 2D model is considered in the paper for the purpose of clear description of the basic procedure of the present approach. Similar 2D treatments can also be found in [12–16] for foam analysis. Strictly speaking, reducing one dimension will cause the honeycomb-type model with open cells along the neglected direction, however, the 2D model can provide a qualitative description of trends and significantly reduce computational cost, compared to 3D model. Actually, the present approach below can be straightforwardly extended for producing 3D foam model having more complex microstructure, without any theoretical difficulty.

### 2.1. Generation of Voronoi diagram

In the present study, 2D Voronoi diagram with the same number of pores as that of the real foam material is generated by randomly placing a set of seed points inside the specific 2D foam region and the number of polygonal cells is controlled by the number of seed points. To avoid very small cells, which are not beneficial to quantitatively investigate the effect of averaged pore size for different form models, the centroid Voronoi technique is employed by iteratively setting the seed points coincide with the centroids of each cell [2]. Figure 2 shows a centroid Voronoi diagram in a square domain with 200 Voronoi polygonal cells. The ratio of maximum and minimum areas of the produced Voronoi cells can be flexibly controlled by setting the number of iterations or iteration tolerance [1]. For example, the area ratio of the biggest and smallest polygonal cells is 15.86 (see Fig. 2a) and 1.46 (see Fig. 2b) after 1 and 50 iterations, respectively. In this work, we focus on the development of the shrinking algorithm to produce the 2D foam, and then quantitatively investigate its effective thermal property caused by different controlling parameters. The presence of too small cells may make the statistics of averaged size of pores meaningless. However, it is worth noting that the developed shrinking algorithm described below is also suitable for the Voronoi diagram with more random arrangement and bigger size difference of cells, as shown in Fig. 2a.

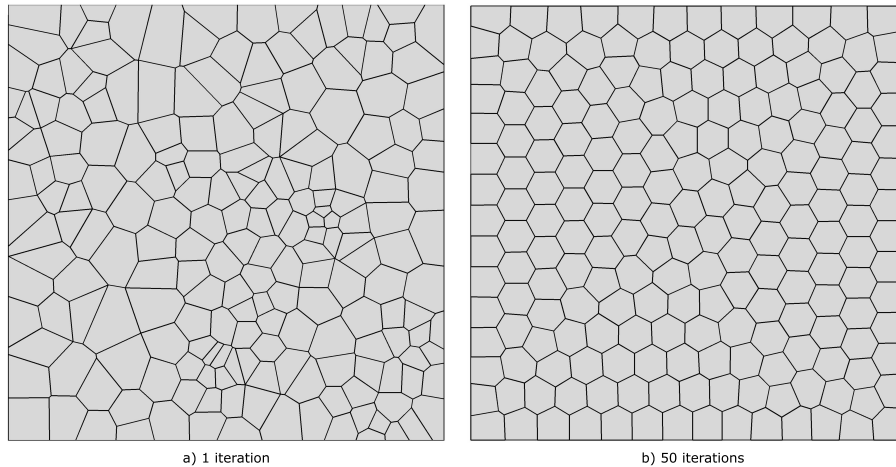


FIG. 2. Schematic diagram of centroid Voronoi tessellations in a square domain with different number of iterations.

### 2.2. Shrinking algorithm for generating closed polygonal pores

Some basic theories related to the convex polygon are described in this section for the Voronoi tessellation as shown in Fig. 2. To do so, three Voronoi polygonal

cells connected to each other are considered and shown in Fig. 3. Referred to the Cartesian coordinate system, the coordinates of the corners and the centroid of one cell is represented by  $(x_i, y_i)$  and  $(x_0, y_0)$ , respectively, as shown in Fig. 3.

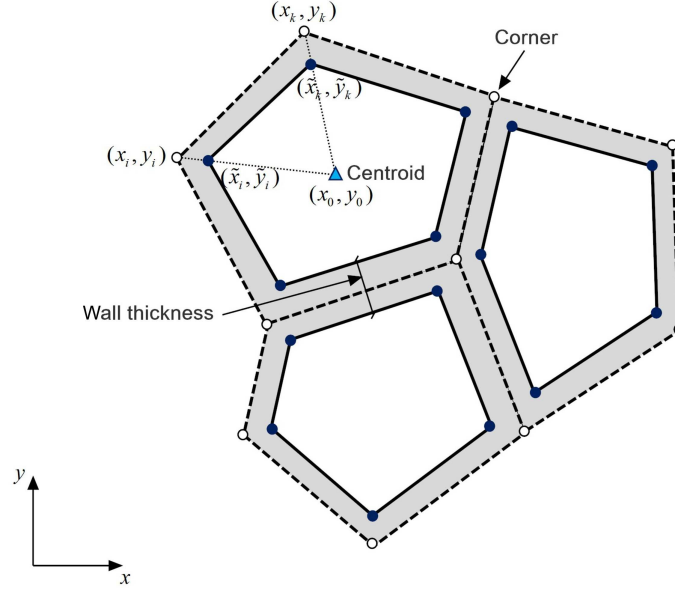


FIG. 3. Schematic diagram of shrinkage of a particular Voronoi polygonal cell.

Assuming that the polygon is shrunk at a specific ratio, i.e.  $\alpha \in (0, 1)$ , the new coordinate  $(\tilde{x}_i, \tilde{y}_i)$  of the corner  $(x_i, y_i)$  can be determined by the following coordinate transformation

$$(2.1) \quad \begin{aligned} \tilde{x}_i - x_0 &= \alpha(x_i - x_0), \\ \tilde{y}_i - y_0 &= \alpha(y_i - y_0), \end{aligned}$$

from which we have

$$(2.2) \quad \begin{aligned} \tilde{x}_i - x_i &= (\alpha - 1)(x_i - x_0), \\ \tilde{y}_i - y_i &= (\alpha - 1)(y_i - y_0). \end{aligned}$$

Similarly, if  $(x_k, y_k)$  is one of the adjacent corners, its new location  $(\tilde{x}_k, \tilde{y}_k)$  after shrinking operation can be derived from Eq. (2.2) as

$$(2.3) \quad \begin{aligned} \tilde{x}_k - x_k &= (\alpha - 1)(x_k - x_0), \\ \tilde{y}_k - y_k &= (\alpha - 1)(y_k - y_0). \end{aligned}$$

Combining Eqs. (2.2) and (2.3) produces

$$(2.4) \quad \begin{aligned} \tilde{x}_k - \tilde{x}_i &= \alpha(x_k - x_i), \\ \tilde{y}_k - \tilde{y}_i &= \alpha(y_k - y_i). \end{aligned}$$

Obviously, Eq (2.4) keeps the line passing points  $(x_i, y_i)$  and  $(x_k, y_k)$  (line 1) and the line passing points  $(\tilde{x}_i, \tilde{y}_i)$  and  $(\tilde{x}_k, \tilde{y}_k)$  (line 2) parallel, due to the following relationship

$$(2.5) \quad \frac{\tilde{x}_k - \tilde{x}_i}{\tilde{y}_k - \tilde{y}_i} = \frac{x_k - x_i}{y_k - y_i}.$$

According to the Heron's formula [26], the triangular area can be expressed in terms of the lengths of the three sides:

$$(2.6) \quad A = \sqrt{s(s-a)(s-b)(s-c)},$$

where  $a$ ,  $b$  and  $c$  are respectively side length of the triangle, and the semiperimeter of the triangle  $s = (a + b + c)/2$ .

For the original triangle consisting of points  $(x_i, y_i)$ ,  $(x_k, y_k)$ , and  $(x_0, y_0)$ , the corresponding lengths of three sides are written by

$$(2.7) \quad \begin{aligned} a &= \sqrt{(x_i - x_0)^2 + (y_i - y_0)^2}, \\ b &= \sqrt{(x_k - x_0)^2 + (y_k - y_0)^2}, \\ c &= \sqrt{(x_i - x_k)^2 + (y_i - y_k)^2}. \end{aligned}$$

Similarly, the side lengths of the shrunk triangle can be given by

$$(2.8) \quad \begin{aligned} \tilde{a} &= \sqrt{(\tilde{x}_i - x_0)^2 + (\tilde{y}_i - y_0)^2}, \\ \tilde{b} &= \sqrt{(\tilde{x}_k - x_0)^2 + (\tilde{y}_k - y_0)^2}, \\ \tilde{c} &= \sqrt{(\tilde{x}_i - \tilde{x}_k)^2 + (\tilde{y}_i - \tilde{y}_k)^2}. \end{aligned}$$

Making use of the basic relations (2.1) and (2.4), we have

$$(2.9) \quad \tilde{a} = \alpha a, \quad \tilde{b} = \alpha b, \quad \tilde{c} = \alpha c,$$

from which the semiperimeter of the shrunk triangle can be written as

$$(2.10) \quad \tilde{s} = (\tilde{a} + \tilde{b} + \tilde{c})/2 = \alpha s.$$

Thus, with the Heron's formula, the area of the shrunk triangle  $\tilde{A}$  is expressed as

$$(2.11) \quad \tilde{A} = \sqrt{\tilde{s}(\tilde{s} - \tilde{a})(\tilde{s} - \tilde{b})(\tilde{s} - \tilde{c})} = \alpha^2 A.$$

Further, the area of the shrunk polygon can be given from the relation (2.11). Thus, for the Voronoi diagram shown in Fig. 2, the area ratio  $\beta$  of the original

polygons over the shrunk polygons, that is the porosity of a foam structure, can be given by

$$(2.12) \quad \beta = \frac{\sum_{n=1}^N \tilde{A}_n}{\sum_{n=1}^N A_n} = \frac{\sum_{n=1}^N \alpha_n^2 A_n}{\sum_{n=1}^N A_n},$$

where  $A_n$  and  $\tilde{A}_n$  are the area of the  $n$ th original and shrunk polygons, respectively.  $\alpha_n$  is the shrinking ratio of the  $n$ th polygon and  $N$  is the number of Voronoi polygonal cells. Apparently, the porosity  $\beta$  and the solid wall thickness can be controlled by adjusting the shrinking ratio  $\alpha_n$  to meet the specified requirement. Specially, when all polygonal cells have the same shrinking ratio  $\alpha$ , we have  $\beta = \alpha^2$  by Eq. (2.12). In the subsequent study, the same shrinking ratio is used for all polygonal cells, unless a special statement is made. For example, in order to obtain the foam material with porosity  $\beta = 0.85$ , we can solve  $\beta = \alpha^2$  to get the required shrinking ratio  $\alpha = 0.922$ .

From the aforementioned procedure, it can be seen that we could generate a controllable closed-cell foam structure with any given values of porosity and wall thickness by adjusting the shrinking ratio. Figure 4 shows an example of the closed-cell foam structure being generated by the present shrinking algorithm with a constant shrinking ratio.

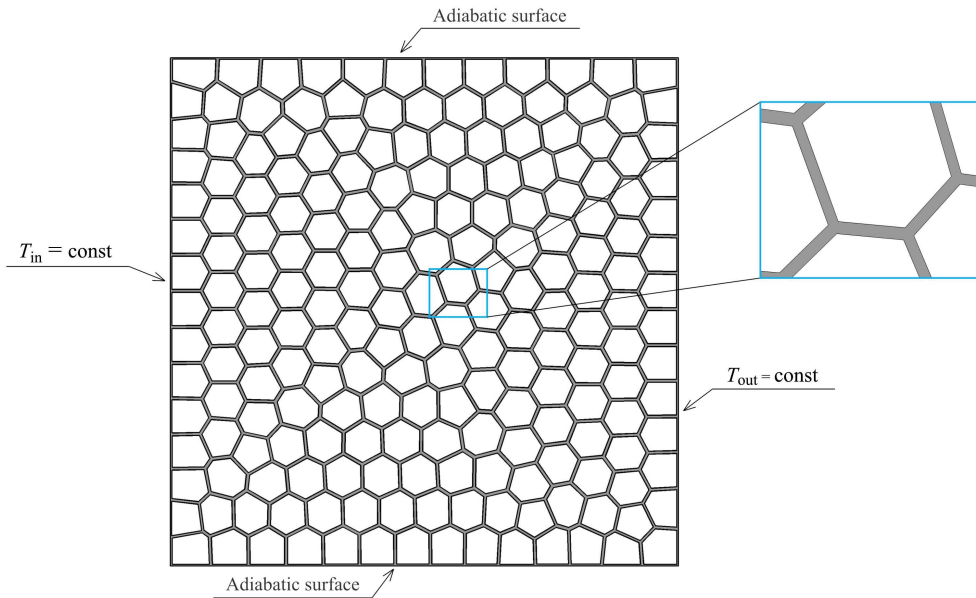


FIG. 4. Example of the generated closed-cell foam structure and the corresponding boundary conditions for heat transfer analysis.

### 3. Effective thermal conductivity of the rebuilt foam structure

#### 3.1. Numerical model

Because the heat transfer of closed-cell metal foams is mainly the heat conduction in the metal matrix and the air fluid inside the pores, the heat convection and radiation can be ignored. This is mainly due to the facts that the closed-cell metal foams usually have relatively small enclosed pores and the ratio of thermal conductivity of the metal phase and the air fluid phase is extremely high [9, 21, 27]. The steady-state heat transfer behavior in a foam structure can, thus, be modelled by the coupled energy balancing equations for the solid and air fluid phases [28]

$$(3.1) \quad \begin{aligned} \nabla \cdot \mathbf{q}_s &= 0, \\ \nabla \cdot \mathbf{q}_f &= 0, \end{aligned}$$

where  $\mathbf{q}_s$  and  $\mathbf{q}_f$  are heat flux vectors in the solid and fluid phases, respectively, which can be expressed in terms of the temperature variable by the Fourier's law,

$$(3.2) \quad \begin{aligned} \mathbf{q}_s &= -k_s \nabla T_s, \\ \mathbf{q}_f &= -k_f \nabla T_f. \end{aligned}$$

In Eq. (3.2),  $k_s$  and  $k_f$  are thermal conductivity of the solid phase and the air fluid phase, respectively, and  $T_s$  and  $T_f$  are respectively the corresponding temperature fields of the solid and air fluid material phase.

Additionally, the continuous conditions for the local thermal equilibrium at the phase interface between solid and fluid require

$$(3.3) \quad \begin{aligned} T_s &= T_f && \text{at phase interface,} \\ \mathbf{q}_s \cdot \mathbf{n} &= \mathbf{q}_f \cdot \mathbf{n} && \text{at phase interface,} \end{aligned}$$

where  $\mathbf{n}$  is the unit normal vector to the interface.

To determine the effective thermal conductivity of the closed-cell foam structure, appropriate boundary conditions should be added to the specific surface of a representative sample [29], i.e. applying the inlet temperature  $T_{\text{in}}$  on the left surface, outlet temperature  $T_{\text{out}}$  on the right surface, and an adiabatic condition on the top and bottom surfaces, as shown in Fig. 4. Here, we assume  $T_{\text{in}} > T_{\text{out}}$  so that we can produce temperature difference between the left and right surfaces to drive heat energy flowing from left to right. Obviously, analytically solving the heat transfer system consisting of Eqs. (3.1)–(3.3) with specific boundary conditions is impossible due to the complex microstructure of foam materials, thus numerical solutions are often resorted to through various numerical methods,

such as the finite element method (FEM) [30–32], the hybrid FEM [33–35], or the boundary element method (BEM) [36, 37]. In this study, the finite element approach is employed to obtain heat flux distribution in the foam structure.

Once the resulting heat flux component along the  $x$ -direction on the right surface  $\Gamma$  is obtained, the effective thermal conductivity of the closed-cell foam material can be given by [3, 38, 39]

$$(3.4) \quad k_e = \frac{\bar{q}_1 L}{T_{\text{in}} - T_{\text{out}}},$$

where the average heat flux component  $\bar{q}_1$  is evaluated as [38]:

$$(3.5) \quad \bar{q}_1 = \frac{1}{L} \left( \int_{L_s} q_{1s} d\Gamma + \int_{L_f} q_{1f} d\Gamma \right)$$

and  $L_s$  and  $L_f$  are the respective surface area of the solid and fluid phases with  $L = L_s + L_f$ .  $L$  denotes the total area of the right surface of the sample foam. Practically, for the present 2D foam structure, the line integral (3.5) is evaluated by the trapezoidal numerical integration.

In this study, the commercial software ABAQUS is employed to investigate the overall thermal conductivities of the rebuilt 2D closed-cell foam models, which are assumed to have unit side length to address the generality of analysis. The solid wall material is assumed to be pure aluminum, which has the thermal conductivity of 237 W/(mK) at the room temperature (20°) [28]. Besides, the thermal conductivity of enclosed air fluid at the room temperature (20°) is taken as 0.02569 W/(mK) [28]. Obviously, the thermal conductivity of the aluminum is 9225 times that of the air in this two-phase foam system. Both the solid wall phase and the air fluid phase are modeled with DC2D8 elements (see ABAQUS element library for details). The analysis begins with a specific higher temperature of 320 K over the left wall and a lower temperature of 300 K over the right wall of the foam.

The porosity of the rebuilt aluminum foam is assumed to be 0.55, 0.65, 0.75, 0.85 and 0.95, respectively, which covers a large range of porosity. Additionally, once the foam porosity is specified, a given pore size can be obtained by adjusting the number of pores. In this work, the number of pores in the foam structure is set to 100, 200 and 300, respectively. As a result, total 15 different foam structures are created in the study, as displayed in Fig. 5. To assess the size difference of these foams, the average radius of pores for each foam structure is defined by

$$(3.6) \quad r_{\text{average}} = \sqrt{\sum_{n=1}^N \tilde{A}_n / (N \times \pi)}.$$

Table 1 illustrates the variation of the average radius of pores in terms of the porosity and the number of pores.

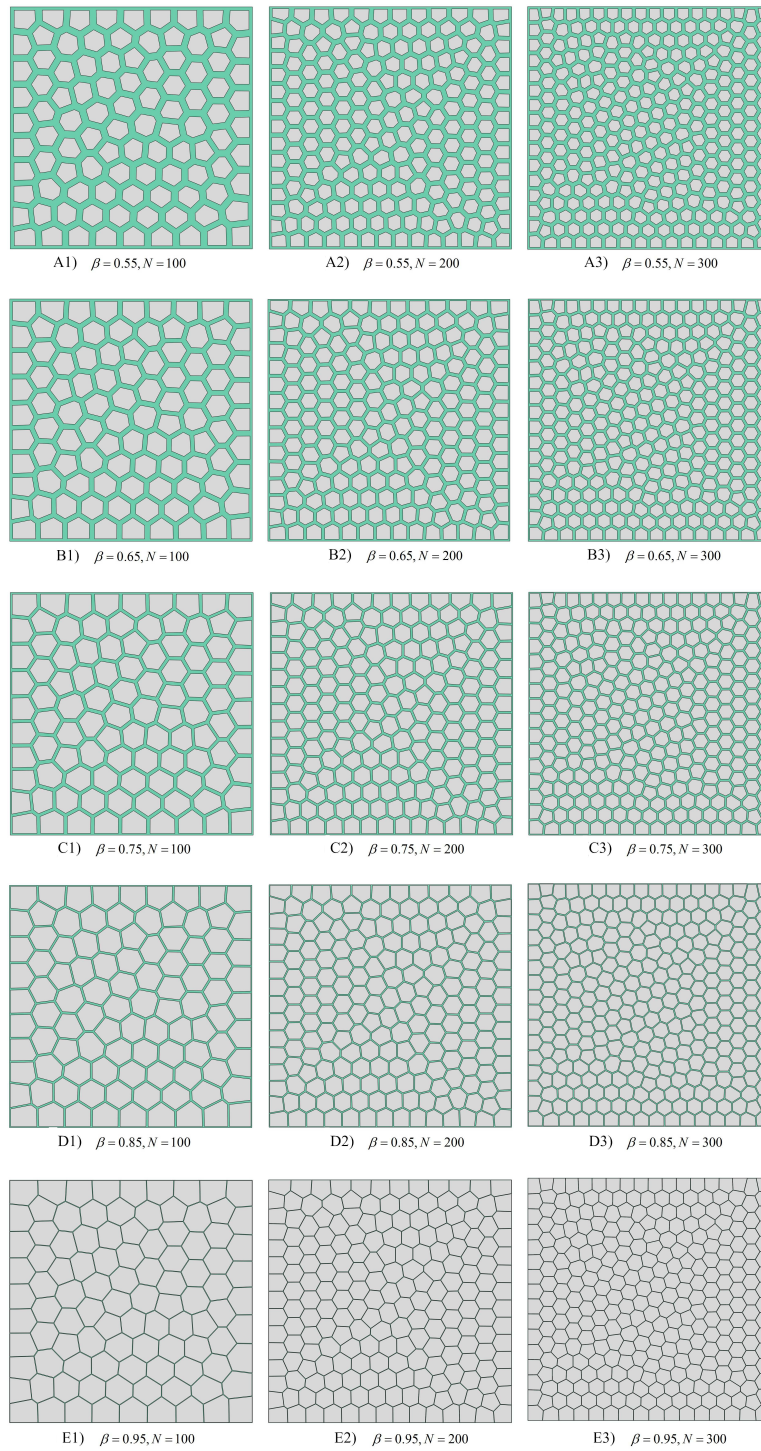


FIG. 5. 15 different foam structures created by the present shrinking algorithm.

**Table 1. Average radius of pores for different foam structures.**

Porosity	Number of pores		
	100	200	300
0.55	0.0418	0.0296	0.0242
0.65	0.0455	0.0322	0.0263
0.75	0.0489	0.0345	0.0282
0.85	0.0520	0.0368	0.0300
0.95	0.0550	0.0389	0.0317

### 3.2. Asymptotic theoretical models

So far, a wide variety of theoretical modes have been developed for prediction of thermal conductivity of closed-cell foams (see [40] for a review report in this area). When the thermal conductivity of the solid phase is far greater than that of the air phase in metal, i.e.  $k_s \gg k_f$ , these models can be simplified. Among these simplified theoretical models, the Parallel-Series, Series-Parallel and Maxwell-Series models overestimate the thermal conductivity of high-porosity foams, while the simplified Bruggemann's model

$$(3.7) \quad \frac{k_e}{k_s} = \left( \frac{\rho_{foam}}{\rho_{solid}} \right)^n = (1 - \beta)^n$$

can give the prediction close to the experimental data [40]. In Eq. (3.7), the symbol  $\rho$  denotes the density, and the exponent  $n = 1.5$  for the Bruggemann's model.

Besides, for the high-porosity metal foams, Kanaun and Babaii Kocheksarai presented the simplest theoretical prediction with the upper and lower limits of thermal conductivity of the foam [41], that is,

$$(3.8) \quad \frac{k_e}{k_s} = \frac{2(1 - \beta)}{3}$$

and

$$(3.9) \quad \frac{k_e}{k_s} = \frac{(1 - \beta)}{3}.$$

Evidently, the actual effective thermal conductivities of metal foam structures with relatively large but finite values of porosity are usually in-between the two asymptotics defined by Eqs. (3.8) and (3.9).

Apart from the above theoretical predictions, GONG *et al.* [42] gave the following expression to model the thermal conductivity of the two-phase porous system (solid and air)

$$(3.10) \quad (1 - \beta) \frac{k_s - k_e}{k_s + 2k_m} + \beta \frac{k_f - k_e}{k_f + 2k_m} = 0,$$

where the value of  $k_m$  is permitted to change for different porous materials to meet the experimental data [42]. Here, the value of  $k_m$  is determined through fitting the present numerical results for the developed metallic foam structure.

#### 4. Results and discussion

In this section, the heat conduction in a metal form, shown in Fig. 5, which is composed of both the solid and air phases, is considered for predicting its thermal conductivity. The steady-state energy balancing equations presented in Section 3.1 are solved numerically over the entire foam RVE region by the standard finite elements method so that we can obtain the temperature fields and their gradients at any point of the two-phase foam. In practical computation, a relatively high mesh density of the foam structure is required to achieve accurate and convergent results such that the maximum relative difference in the predicted thermal conductivity is less than a specified tolerance, say 0.05%. Table 2 illustrates four meshes by giving different approximated element sizes for the foam structure A1 shown in Fig. 5. It is found that the relative difference decreases from 0.485% to 0.044%, as the element size, is reduced from 0.0136 to 0.0034. The approximated element size 0.0034 can produce extra fine mesh in the computational domain, which can give better accuracy, as indicated in Table 2.

**Table 2. Variations of results in mesh sensitivity analysis.**

	Mesh configurations	$k_e$
Mesh1	Approximated element size: 0.0136	67.5234
	Number of elements: 6387	
	Number of nodes: 19454	
Mesh2	Approximated element size: 0.0068	67.1959
	Number of elements: 29977	
	Number of nodes: 90520	
Mesh3	Approximated element size: 0.0045	67.2561
	Number of elements: 68643	
	Number of nodes: 206818	
Mesh4	Approximated element size: 0.0034	67.2268
	Number of elements: 120238	
	Number of nodes: 361891	

Additionally, from the above procedure, it is noted that the present shrinking algorithm just produces the foam structure with fully closed pores. Practically, the pores close to the foam boundary are permitted to be open. Here, a simple comparison is made for these two different cases. For convenience, the foam model D2 in Fig. 5 is modified by expanding related edges of pores on the boundary,

as shown in Fig. 6, to create the foam structure with open boundary pores. The porosity of the resulted foam is 0.861. Correspondingly, a new foam model with fully closed pores is created to hold the same porosity by the present shrinking algorithm. Results in Table 3 indicate that there is a negligible difference between the values of the effective thermal conductivity of the two foam structures. Thus, the effect of open boundary pores on the thermal conductivity of foam can be ignored in practice, and in the following analysis, we just pay our attention to the foam materials with fully-closed pores.

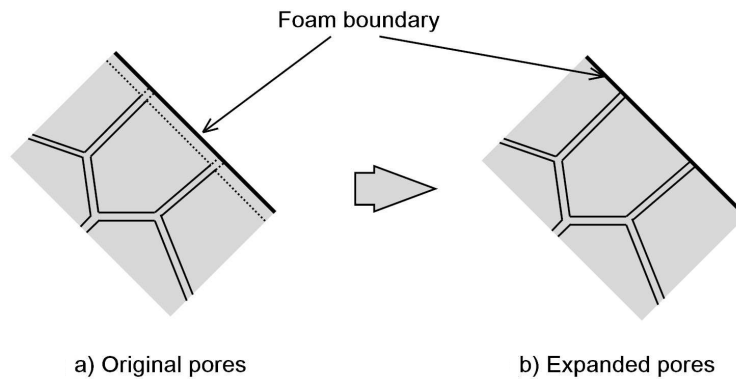


FIG. 6. Expanding procedure for producing open boundary pores.

**Table 3. Comparison of the two foams with same porosity.**

	Approximated element size	Number of elements	$k_e$
Foam with open boundary pores	$2.0 \times 10^{-3}$	342481	17.5943
Foam with fully closed pores	$1.2 \times 10^{-3}$	949412	17.5465

#### 4.1. Effect of the porosity of foam

It should be noted that the thermal property of metal foams depends on both the porosity and the pore size. In this section, the effects of the porosity and the pore size on the effective thermal conductivity of the foam are investigated. Table 4 lists the finite element solutions for fifteen different foam structures generated using the procedure described above. It is seen that the pore size controlled by the number of pores has little effect on the effective thermal properties of the foams when the porosity keeps constant. For the present medium-high porosity, all relative derivations between the maximum and minimum values are less than 0.5%. In addition, the results in Table 4 indicate that the effective thermal

conductivity of the present closed-cell foams decreases with the increase in the porosity, as expected.

**Table 4. Numerical results of the effective thermal conductivity for different foam structures.**

Porosity	Number of pores $n$			Relative derivation	Average
	100	200	300		
0.55	67.2268	67.2763	67.2803	0.0795%	67.2611
0.65	49.2008	49.2777	49.2666	0.1561%	49.2484
0.75	33.3085	33.3353	33.3024	0.0987%	33.3154
0.85	19.0071	18.9991	18.9632	0.2310%	18.9898
0.95	6.0579	6.0563	6.0794	0.3800%	6.0645

On the other hand, to verify the present numerical results, the theoretical predictions obtained using Eqs. (3.7), (3.8) and (3.9) as well as the available experimental results [40] are plotted in Fig. 7, from which it is clearly shown that the numerical predictions of the normalized effective thermal conductivities of the foam structure decrease nonlinearly with the increase of porosity and the values are in-between the upper and lower limits obtained from Eqs. (3.8) and (3.9). Besides, the experimental results and the theoretical results from the Bruggemann's model are all in-between the upper and lower limits. Moreover, the Bruggemann's model can provide acceptable fit to the numerical and experimental results.

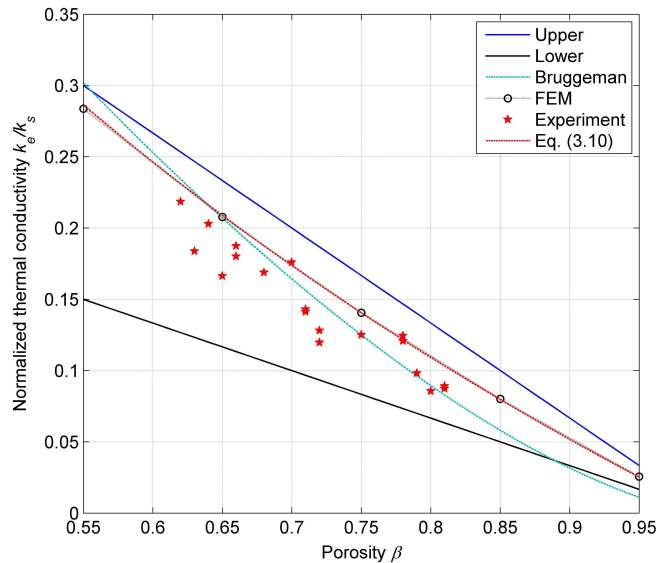


FIG. 7. Comparison of numerical results and other available solutions.

In addition, the most obstacle of using the expression in Eq. (3.10) is to determine the parameter  $k_m$ , whose value depends on the property of the porous material [42]. To bypass this, the data fitting technique is employed based on the obtained numerical results in Table 4, and  $k_m = 113.943$  W/(mK) is obtained for the present closed-cell foam models. With this value, the expression in Eq. (3.10) can provide results which match well with the numerical results obtained for the present medium-high porosity, as shown in Fig. 7.

#### 4.2. Effect of the thermal conductivity of solid material

In this section, dependence of the effective thermal conductivity of the foam structure on the matrix material is investigated. To do this, two values of  $\beta = 0.65$  and  $\beta = 0.85$  covering medium and high porosity are used. The thermal conductivity of the solid matrix material is assumed to be changed in the range  $[0.2, 400]$  W/(mK), which covers most of materials commonly used in engineering, from low heat conduction material like cement to high heat conduction material like pure copper. The number of pores is chosen as 200 for simplification. Figure 8 illustrates the variation of the effective thermal conductivity  $k_e$  of the foam with respect to  $k_s$ . It can be seen from Fig. 8 that the effective thermal conductivity of the foam increases linearly with the increase of thermal conductivity of the solid matrix phase. This can be attributed to the big difference of thermal conductivity of solid phase and air phase, which is also the basis of Eqs. (19)–(21).

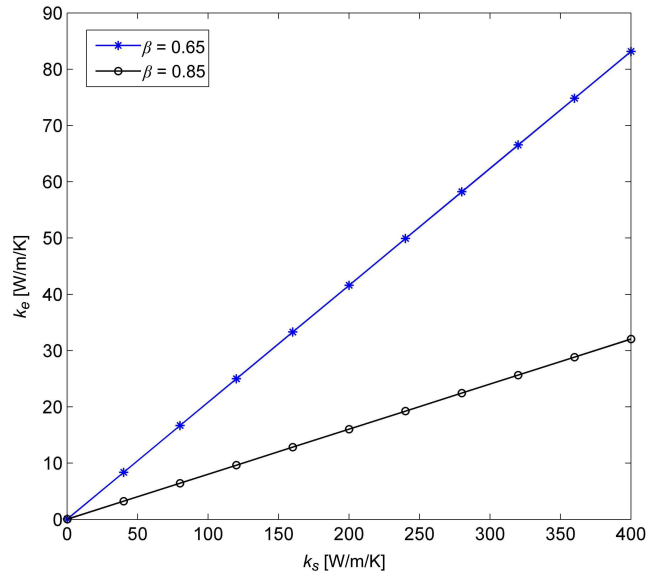


FIG. 8. Variation of the effective thermal conductivity of the foam with that of the solid matrix phase.

## 5. Conclusions

In this study, the two-dimensional closed-cell foam model based on the Voronoi shrinking technique is geometrically constructed and then numerically analyzed for predicting the thermal conductivity of the foam. It is found that the morphological parameters of the foam microstructure such as porosity and wall thickness can be easily and precisely achieved by adjusting the shrinking ratio. The present random foam model based on Voronoi tessellation shrinking is verified using the available theoretical and experimental results. Subsequently, the effects of porosity, number of pores and solid wall material on the effective thermal conductivity of the foam are investigated. It is observed that the effective thermal conductivity of the rebuilt foam model nonlinearly decreases with the increase of the porosity, while it linearly relates to the thermal conductivity of solid matrix material when there is a big difference of thermal property of solid material and air enclosed in the pores. Besides, we find that the effective thermal conductivity of the foam is not sensitive to the minor change from the fully-closed foam model to that with open boundary pores under the same porosity.

## Acknowledgements

The work described in this paper was partially supported by the National Natural Science Foundation of China (Grant nos. 11472099 and 11372100) and the fund of the State Key Laboratory of Structural Analysis for Industrial Equipment in the Dalian University of Technology (Grant no. GZ1610).

## References

1. C. TALISCHI, G.H. PAULINO, A. PEREIRA, I.F.M. MENEZES, *PolyMesher: a general-purpose mesh generator for polygonal elements written in Matlab*, Structural and Multidisciplinary Optimization, **45**, 3, 309–328, 2012.
2. Q. DU, V. FABER, M. GUNZBURGER, *Centroidal Voronoi tessellations: applications and algorithms*, SIAM review, **41**, 4, 637–676, 1999.
3. H. WANG, Q.-H. QIN, Y. XIAO, *Special n-sided Voronoi fiber/matrix elements for clustering thermal effect in natural-hemp-fiber-filled cement composites*, International Journal of Heat and Mass Transfer, **92**, 228–235, 2016.
4. H. WANG, Q.-H. QIN, *Voronoi polygonal hybrid finite elements with boundary integrals for plane isotropic elastic problems*, International Journal for Applied Mechanics, **9**, 3, 1750031, 2017.
5. N. DUKHAN, *Metal Foams: Fundamentals and Applications*, DEStech Publications, Lancaster, 2013.
6. C. LAUTENSACK, *Fitting three-dimensional Laguerre tessellations to foam structures*, Journal of Applied Statistics, **35**, 9, 985–995, 2008.

7. L.Q. TANG, X.P. SHI, L. ZHANG, Z.J. LIU, Z.Y. JIANG, Y.P. LIU, *Effects of statistics of cell's size and shape irregularity on mechanical properties of 2D and 3D Voronoi foams*, *Acta Mechanica*, **225**, 4–5, 1361–1372, 2014.
8. C. REDENBACH, I. SHKLYAR, H. ANDRÄ, *Laguerre tessellations for elastic stiffness simulations of closed foams with strongly varying cell sizes*, *International Journal of Engineering Science*, **50**, 1, 70–78, 2012.
9. Z.Q. LI, J.J. ZHANG, Z.H. WANG, Y.Z. SONG, L.M. ZHAO, *Study on the thermal properties of closed-cell metal foams based on Voronoi random models*, *Numerical Heat Transfer, Part A: Applications*, **64**, 12, 1038–1049, 2013.
10. Z.Q. LI, J.J. ZHANG, J.H. FAN, Z.H. WANG, L.M. ZHAO, *On crushing response of the three-dimensional closed-cell foam based on Voronoi model*, *Mechanics of Materials*, **68**, 85–94, 2014.
11. C. BARBIER, P.M. MICHAUD, D. BAILLIS, J. RANDRIANALISOA, A. COMBESCURE, *New laws for the tension/compression properties of Voronoi closed-cell polymer foams in relation to their microstructure*, *European Journal of Mechanics-A/Solids*, **45**, 110–122, 2014.
12. D. LI, L. DONG, J.-H. YIN, R.S. LAKES, *Negative Poisson's ratio in 2D Voronoi cellular solids by biaxial compression: a numerical study*, *Journal of Materials Science*, **51**, 14, 7029–7037, 2016.
13. M.J. SILVA, W.C. HAYES, L.J. GIBSON, *The effects of non-periodic microstructure on the elastic properties of two-dimensional cellular solids*, *International Journal of Mechanical Sciences*, **37**, 11, 1161–1177, 1995.
14. M.J. SILVA, L.J. GIBSON, *The effects of non-periodic microstructure and defects on the compressive strength of two-dimensional cellular solids*, *International Journal of Mechanical Sciences*, **39**, 5, 549–563, 1997.
15. C. CHEN, T.J. LU, N.A. FLECK, *Effect of imperfections on the yielding of two-dimensional foams*, *Journal of the Mechanics and Physics of Solids*, **47**, 11, 2235–2272, 1999.
16. H.X. ZHU, J.R. HOBDELL, A.H. WINDLE, *Effects of cell irregularity on the elastic properties of 2D Voronoi honeycombs*, *Journal of the Mechanics and Physics of Solids*, **49**, 4, 857–870, 2001.
17. T. LU, C. CHEN, *Thermal transport and fire retardance properties of cellular aluminium alloys*, *Acta Materialia*, **47**, 5, 1469–1485, 1999.
18. G.-Y. LU, B.-Y. SU, Z.-Q. LI, Z.-H. WANG, W.-D. SONG, H.-P. TANG, *Thermal properties of closed-cell aluminum foam with circular pores*, *Thermal Science*, **18**, 5, 1619–1624, 2014.
19. T. SADOWSKI, B. PANKOWSKI, *Numerical modelling of two-phase ceramic composite response under uniaxial loading*, *Composite Structures*, **143**, 388–394, 2016.
20. J. KADKHODAPOUR, S. RAEISI, *Micro–macro investigation of deformation and failure in closed-cell aluminum foams*, *Computational Materials Science*, **83**, 137–148, 2014.
21. X.L. ZHU, S.G. AI, X.F. LU, X. LING, L.X. ZHU, B. LIU, *Thermal conductivity of closed-cell aluminum foam based on the 3D geometrical reconstruction*, *International Journal of Heat and Mass Transfer*, **72**, 242–249, 2014.

22. T. FIEDLER, E. SOLÓRZANO, F. GARCIA-MORENO, A. ÖCHSNER, I.V. BELOVA, G.E. MURCH, *Computed tomography based finite element analysis of the thermal properties of cellular aluminium*, *Materialwissenschaft und Werkstofftechnik*, **40**, 3, 139–143, 2009.
23. K.K. BODLA, J.Y. MURTHY, S.V. GARIMELLA, *Microtomography-based simulation of transport through open-cell metal foams*, *Numerical Heat Transfer, Part A: Applications*, **58**, 7, 527–544, 2010.
24. T. WEJRZANOWSKI, J. SKIBINSKI, J. SZUMBARSKI, K.J. KURZYDŁOWSKI, *Structure of foams modeled by Laguerre–Voronoi tessellations*, *Computational Materials Science*, **67**, 216–221, 2013.
25. R. JAFARI, M. KAZEMINEZHAD, *Microstructure generation of severely deformed materials using Voronoi diagram in Laguerre geometry: Full algorithm*, *Computational Materials Science*, **50**, 9, 2698–2705, 2011.
26. H.S.M. COXETER, *Introduction to Geometry*, Wiley, New York, 1969.
27. D.H. XIA, S.S. GUO, L. REN, *Study of the reconstruction of fractal structure of closed-cell aluminum foam and its thermal conductivity*, *Journal of Thermal Science*, **21**, 1, 77–81, 2012.
28. H.D. BAEHR, K. STEPHAN, *Heat and Mass Transfer*, Springer, Berlin, 2006.
29. Q.H. QIN, M.V. SWAIN, *A micro-mechanics model of dentin mechanical properties*, *Bio-materials*, **25**, 20, 5081–5090, 2004.
30. K.J. BATHE, *Finite Element Procedures*, Prentice Hall, New Jersey, 1996.
31. Q.H. QIN, *Hybrid Trefftz finite-element approach for plate bending on an elastic foundation*, *Applied Mathematical Modelling*, **18**, 6, 334–339, 1994.
32. M. DHANASEKAR, J. HAN, Q.H. QIN, *A hybrid-Trefftz element containing an elliptic hole*, *Finite Elements in Analysis and Design*, **42**, 14, 1314–1323, 2006.
33. Q.H. QIN, H. WANG, *MATLAB and C Programming for Trefftz Finite Element Methods*, CRC Press, New York, 2008.
34. Q.H. QIN, *Hybrid-Trefftz finite element method for Reissner plates on an elastic foundation*, *Computer Methods in Applied Mechanics and Engineering*, **122**, 3–4, 379–392, 1995.
35. H. WANG, Q.H. QIN, *FE approach with Green’s function as internal trial function for simulating bioheat transfer in the human eye*, *Archives of Mechanics*, **62**, 6, 493–510, 2010.
36. Q.H. QIN, Y.W. MAI, *BEM for crack-hole problems in thermopiezoelectric materials*, *Engineering Fracture Mechanics*, **69**, 5, 577–588, 2002.
37. X.W. GAO, T.G. DAVIES, *Boundary Element Programming in Mechanics*, Cambridge University Press, Cambridge, 2002.
38. J. RANDRIANALISOA, D. BAILLIS, C.L. MARTIN, R. DENDIEVEL, *Microstructure effects on thermal conductivity of open-cell foams generated from the Laguerre–Voronoi tessellation method*, *International Journal of Thermal Sciences*, **98**, 277–286, 2015.
39. H. WANG, X.J. ZHAO, J.S. WANG, *Interaction analysis of multiple coated fibers in cement composites by special n-sided interphase/fiber elements*, *Composites Science and Technology*, **118**, 117–126, 2015.

40. E. SOLÓRZANO, J.A. REGLERO, M.A. RODRÍGUEZ-PÉREZ, D. LEHMHUS, M. WICHMANN, J.A. DE SAJA, *An experimental study on the thermal conductivity of aluminium foams by using the transient plane source method*, International Journal of Heat and Mass Transfer, **51**, 25, 6259–6267, 2008.
41. S. KANAUN, S.B. KOCHESERAI, *Conductive properties of foam materials with open or closed cells*, International Journal of Engineering Science, **50**, 1, 124–131, 2012.
42. L.L. GONG, Y.H. WANG, X.D. CHENG, R.F. ZHANG, H.P. ZHANG, *A novel effective medium theory for modelling the thermal conductivity of porous materials*, International Journal of Heat and Mass Transfer, **68**, 295–298, 2014.

*Received May 17, 2017; revised version September 18, 2017.*

---